Cryo-EM structures of the active NLRP3 inflammasome disc

Le Xiao[1,2], **Venkat Giri Magupalli**[1,2], **Hao Wu**[1,2,✉]

[1]Department of Biological Chemistry and Molecular Pharmacology, Harvard Medical School, Boston, MA, USA.

[2]Program in Cellular and Molecular Medicine, Boston Children's Hospital, Boston, MA, USA.

Abstract

Inflammasomes are cytosolic innate immune complexes that activate caspase-1 following detection of pathogenic and endogenous dangers[1–5], and NACHT-, leucine-rich repeat (LRR)- and pyrin domain (PYD)-containing protein 3 (NLRP3) is an inflammasome sensor of membrane damage highly important in regard to the induction of inflammation[2,6,7]. Here we report cryogenic electron microscopy structures of disc-shaped active NLRP3 oligomers in complex with adenosine 5′-O-(3-thio)triphosphate, the centrosomal NIMA-related kinase 7 (NEK7) and the adaptor protein ASC, which recruits caspase-1. In these NLRP3–NEK7–ASC complexes, the central NACHT domain of NLRP3 assumes an ATP-bound conformation in which two of its subdomains rotate by about 85° relative to the ADP-bound inactive conformation[8–12]. The fish-specific NACHT-associated domain conserved in NLRP3 but absent in most NLRPs[13] becomes ordered in its key regions to stabilize the active NACHT conformation and mediate most interactions in the disc. Mutations on these interactions compromise NLRP3-mediated caspase-1 activation. The N-terminal PYDs from all NLRP3 subunits combine to form a PYD filament that recruits ASC PYD to elicit downstream signalling. Surprisingly, the C-terminal LRR domain and the LRR-bound NEK7 do not participate in disc interfaces. Together with previous structures of an inactive NLRP3 cage in which LRR–LRR interactions play an important role[8–11], we propose that the role of NEK7 is to break the inactive cage to transform NLRP3 into the active NLRP3 inflammasome disc.

NACHT-, leucine-rich repeat (LRR)- and pyrin domain (PYD)-containing protein 3 (NLRP3) belongs to the NLR family and is a versatile inflammasome sensor that detects a range of pathogenic invasions and damage-associated stimuli including the bacterial toxin nigericin, extracellular ATP, amyloid-β fibrils and uric acid crystals. These stimuli converge to cellular K^+ efflux, a common trigger for NLRP3 activation[2,14]. The fish-specific NACHT-associated (FISNA) domain of NLRP3, between the PYD and NACHT domains (Fig. 1a), has been implicated as a conformational switch in NLRP3 activation following induction of K^+ efflux using a cellular bioluminescence resonance energy transfer assay[13]. Previous studies also suggest that, following triggering, NLRP3 traffics on transGolgi network (TGN) marker-containing vesicles along the microtubule to the microtubule organizing centre (MTOC)[15–17]. Activated NLRP3 recruits ASC, which is the adaptor apoptosis-associated speck-like protein containing a caspase recruitment domain (CARD), through PYD–PYD interactions, and ASC in turn recruits and activates caspase-1 through CARD–CARD interactions[1,18–21] to form the NLRP3 inflammasome as a singular speck at the MTOC[15,17]. Intriguingly, centrosomal NIMA-related kinase 7 (NEK7), important in mitosis, has been identified as a scaffolding protein in NLRP3 activation independent of its kinase activity[22–24]. Activated caspase-1 cleaves the proinflammatory cytokines pro-IL-1β and pro-IL-18 and the pore-forming protein gasdermin D (GSDMD) to mediate mature cytokine release and pyroptotic cell death[25–32]. NLRP3 mutations cause autoinflammatory diseases[33,34], and NLRP3 hyperactivation is associated with many common conditions including cardiovascular, metabolic and neurodegenerative diseases[2,35]. Our structures of the NLRP3–NEK7–ASC complex in the active state shed light on NLRP3 inflammasome assembly and activation to mount host defences and restore cellular homeostasis, and provide a platform for understanding and targeting NLRP3-related human diseases.

Structure determination

We co-expressed full-length NLRP3 and NEK7 (Fig. 1a) in Expi293F cells, stimulated the cells with nigericin—a known NLRP3 activator that we used previously[15]—and purified the NLRP3–NEK7 complex using the FLAG tag on NEK7. Gel filtration chromatography showed two peaks, but neither gave rise to large homogeneous particles under negative-staining EM (Extended Data Fig. 1a–c). Because ATP was reported previously as essential for activation of the NLRP3 inflammasome[36], we added the ATP analogue adenosine 5′-O-(3-thio)triphosphate (ATPγS) and $MgCl_2$ with the goal of locking NLRP3 in an active conformation. Gel filtration chromatography of the NLRP3–NEK7 complex in the presence of ATPγS showed larger complexes but the sample remained heterogeneous (Extended Data Fig. 1d–h). We wondered whether ASC is required for assembly of the NLRP3 inflammasome, and thus expressed and purified the PYD of ASC (Fig. 1a) as described previously[18]. We then added ASC PYD to the NLRP3–NEK7 complex at a 1:1 molar ratio. The mixture was incubated overnight with tobacco etch virus protease to remove the maltose-binding protein (MBP) tags on NLRP3 and ASC PYD, and was then subjected to gel filtration chromatography. The sharp peak near the void elution position contained all three proteins although ASC PYD appeared to be substoichiometric, probably because of the precipitation of large ASC PYD filaments or its retention by the filter membrane in the gel filtration column (Extended Data Fig. 2a–c). Negative-staining EM showed largely

homogeneous particles of around 30 nm in diameter (Fig. 1b), suggesting that ASC PYD co-assembles with NLRP3 to complete its activation. Addition of ASC PYD to the NLRP3–NEK7 complex at a 10:1 overstoichiometric molar ratio resulted in some particles having long filamentous tails (Fig. 1c), which confirms the ability of the NLRP3 inflammasome we reconstituted to nucleate ASC PYD polymerization.

We collected cryogenic electron microscopy (cryo-EM) data on the NLRP3–NEK7–ASC complex (Extended Data Fig. 2d). Two-dimensional (2D) classification showed full discs on top/bottom views (Fig. 1d), each containing ten or 11 subunits (Fig. 2e–f). We solved cryo-EM structures of the tenfold disc (C10) at 3.4 Å resolution, and of the 11-fold (C11) disc at 3.8 Å resolution (Extended Data Figs. 3 and 4a,b and Extended Data Table 1). Local-resolution distributions showed that the centre of the discs, which represents the key region for NLRP3 oligomerization, had the best resolution of around 2.8 Å (Extended Data Fig. 4a). Some of the complexes are partial discs, as shown by 2D classification (Fig. 1d), and three-dimensional reconstruction using particles from these classes resulted in a cryo-EM map containing mainly five subunits at 3.8 Å resolution (Extended Data Figs. 3 and 4c and Extended Data Table 1).

We observed tubular density for the PYD filament of NLRP3 and ASC from side views of the C10 and C11 maps (Extended Data Fig. 5a,b); the density, however, was weak, probably because of the different symmetry of the filament from the rest of the domains, and the flexible linker after the PYD. The five-subunit map showed only diffuse density in this region (Extended Data Fig. 5c), suggesting that more subunits in a disc may be required for effective recruitment of ASC by nucleation of ASC PYD filament formation. Because some particles contain stacked discs (Fig. 1b), which are linked together by the NLRP3 PYD filaments from the opposing discs, the 2D classes showed a longer PYD filament in the middle (Fig. 1d), from which we obtained a 3.3-Å-resolution structure of the NLRP3 PYD filament by helical reconstruction (Extended Data Figs. 3 and 5d and Extended Data Table 1). This NLRP3 filament structure is similar to that published previously[10].

Because of enhanced resolution, we will focus on the atomic model built for the C10 disc of the active NLRP3 inflammasome consisting of ten full-length NLRP3 and ten full-length NEK7, using previous NLRP3 (ref. [8]) and full-length NEK7 (ref. [37]) structures as initial models. In addition, approximately 20 PYD subunits in a filament fit well with the height of the central tubular density visible from the side view of the disc, and we thus built a cofilament consisting of ten NLRP3 PYD and ten recruited ASC PYD[18] to complete the NLRP3–NEK7–ASC complex. Representative regions of cryo-EM density superimposed with the final C10 model are shown in Extended Data Fig. 6.

Overall structure of the NLRP3 disc

The cryo-EM structure showed that the individual NLRP3 subunit consists of the flexibly linked N-terminal PYD, the FISNA domain[13], the canonical NACHT domain comprising the ATPγS-bound nucleotide-binding domain (NBD), helical domain 1 (HD1), a winged helix domain (WHD) and helical domain 2 (HD2) and the C-terminal LRR domain (Figs. 1a and 2a). Ten such subunits form a large flower-shaped disc of diameter about 32 nm

from top and bottom views, in which the FISNA–NACHT domains interact near the centre of the disc and the LRR domains and bound NEK7 extend away from the centre (Fig. 2b–e). Thus, neither NEK7 nor the NLRP3 LRR domain participates in direct interactions in the disc assembly. At the FISNA–NACHT region of the assembly, the top view shows prominent NBD, WHD and HD2 whereas the bottom view shows more prominent FISNA and HD1 (Fig. 2b). The acidic loop (residues 686–725) situated at the LRR–LRR interface in a decameric cage structure of human NLRP3 (ref. [10]) but disordered in all other human and mouse NLRP3 structures[8,9,11], is also disordered in the activated NLRP3 structure. The side view of the disc highlights the NLRP3–ASC PYD cofilament complex (Fig. 2c,d).

Conformational change at FISNA and NACHT

The conformation of active NLRP3 shows marked differences from those of inactive NLRP3 solved in PYD-deleted form in complex with NEK7 (ref. [8]), in full-length cage forms[9–11], in PYD-deleted hexameric form[11] or in NACHT alone in complex with an inhibitor[12]. When the FISNA–NBD–HD1 regions of NLRP3 in the two states are aligned, the WHD–HD2–LRR module needs to rotate by approximately 85.4° along an axis at the junction between HD1 and WHD to turn from the inactive to the active state (Fig. 3a). This structural change is roughly a rigid body rotation because the FISNA–NBD–HD1 and WHD–HD2–LRR modules align well in gross conformations between the inactive and active states (Fig. 3b and Extended Data Fig. 7a). At the overall structural level, the LRR domain and NEK7 of the inactive NLRP3–NEK7 complex would have been in conflict with a neighbouring NLRP3 molecule in the active disc (Extended Data Fig. 7b).

In NLRC4, the only example among NLRs for which both inactive and active structures are available, the WHD–HD2–LRR module needs to rotate by about 87.5° along a similar axis to change from the inactive state to active[38–40]. Whereas rotations in NLRP3 and NLRC4 are quite similar, the active states of NLRP3 and NLRC4 are considerably different (Extended Data Fig. 7c), resulting in inaccurate modelling of the active NLRP3 disc[8] from the known structure of the NLRC4 disc[38,39].

The exception to rigid body rotation in conformational change is the FISNA domain, which undergoes pronounced structural changes (Fig. 3c). A region in the middle of the FISNA domain disordered in the inactive conformation becomes an α-helix (helix 2, residues 176–202), and disordered loop 1 (residues 151–163) becomes ordered in the active conformation (Fig. 3c). The disorder of helix 2 and loop 1 in the inactive conformation is because of conflict with LRR–NEK7 and WHD, respectively, if these regions were ordered (Fig. 3d). In addition, loop 2 (residues 212–217) undergoes conformational change (Fig. 3c). These structural changes indicate that the FISNA domain plays an important role in the activation of NLRP3. Whereas the presence of FISNA is unique to NLRP3 and NLRP12 among NLRPs[13], structural alignment showed that NLRC4 and NAIP5 (refs. [41,42]) also have a FISNA domain that is, however, similar to the inactive conformation of the NLRP3 FISNA domain, with a deletion of helix 2 (Extended Data Fig. 7d).

ATP binding and NLRP3 disease mutations

Conformational changes at the FISNA and NACHT domains are accompanied by exchange of ADP in the inactive conformation to ATPγS (mimicking ATP) in the active conformation. Whereas the cryo-EM density for ATPγS is clear (Extended Data Fig. 6h), that for Mg^{2+} is weak for reasons unknown. In the active state, ATPγS is surrounded mainly by NBD but also by FISNA and, more peripherally, by HD1 and WHD (Fig. 3e). For NBD, certain main-chain amide nitrogen atoms of the Walker A motif[43] (or P-loop, 226-GAAGIGKTI-234), and the side chains of K232 of the Walker A motif and R351 of the sensor 1 motif[43] (346-LLITTR-351), interact with the phosphate groups of ATPγS. D302 of the Walker B motif[43] (298-LFLMDGFDE-306) helps in coordinating the bound Mg^{2+} ion with β- and γ-phosphates. For the FISNA domain, R154 (loop 1) forms a hydrogen bond with the O_3 atom of the ribose, and T169 main and side chains interact with N_1 and N_6 atoms of the adenine ring. If ATP is placed in the ADP-bound, inactive state, the conserved H522 residue in WHD—important for ADP binding—would come into conflict with ATPγS (Fig. 3f), rationalizing the required change in WHD location in the ATP-bound, active state.

Although it has been speculated that all NLRs can switch between an ADP-bound inactive conformation and an ATP-bound active conformation, there has not been any structural observation of both states other than that observed here in NLRP3. For NLRC4, the only example among NLRs for which both inactive and active structures are available, no bound nucleotide was captured in the active state although the inactive state binds ADP[38–40]. In the NLR-related protein Apaf-1, the domain rotation at the junction between HD1 and WHD between the two states is around 180° (ref. [44]) and in CED-4, the Apaf-1 orthologue in *Caenorhabditis elegans*, no conformational change in the ATPase region was observed because the inactive state is already bound to ATP but oligomerization is prevented by the bound inhibitor CED-9 (refs. [45,46]).

To investigate the mechanism of NLRP3-related autoinflammation, we mapped disease mutations in cryopyrin-associated periodic syndromes (CAPS)[34]—familial cold autoinflammatory syndrome 1, Muckle–Wells syndrome and chronic infantile neurologic cutaneous and articular syndrome—onto the active NLRP3 structure (Extended Data Fig. 8a,b). Within the FISNA domain, residue I174 at the I174T mutation site interacts with the NBD and engages the V200 residue at the V200M mutation site that was disordered in the inactive conformation; both I174 and V200 can stabilize the FISNA domain in the active conformation. T438I and A441V/T mutations are located at the beginning of the WHD, near the pivot point for the activation of conformational change, which may cause auto-activation of NLRP3. Similar to a previous report[8], most other CAPS mutations are located near the nucleotide-binding site in the NBD, including R262W/L/P, L266H, D305N/G, L307P, T350M and A354V. These mutations may either destabilize the inactive conformation or stabilize the active conformation of NLRP3.

FISNA domain at the NLRP3 interface

There are three major elements of interaction at an NLRP3–NLRP3 interface, and we named the two neighbouring NLRP3 molecules A and B to facilitate the analysis—as we did

for the NLRC4 inflammasome[38] (Fig. 4a–c). First, FISNA loop 1 of NLRP3[B] interacts primarily with the NBD and FISNA domain of the neighbouring NLRP3[A]. Second, FISNA loop 2 of NLRP3[A] interacts with FISNA helix 1 of NLRP3[B]. Third, a region in NLRP3[A] WHD becomes an ordered β-hairpin loop (Extended Data Fig. 8c) and interacts with NLRP3[B] HD1. These interactions have a strong electrostatic component, with the NLRP3[A] interaction surface being largely acidic and NLRP3[B] interaction surface largely basic (Fig. 4d). By contrast, the corresponding NLRC4[A] surface is largely basic and NLRC4[B] largely acidic[38].

Quantitative analysis using PDBePISA for exploration of macromolecular interfaces[47] identified FISNA domain residues R147 from helix 1, E152, N155 and R157 from loop 1, D213 from loop 2, K166 and E176 from other regions, NBD residues Q359 and H364, HD1 residue Q424 and WHD residues Q509 and D513 as contributing substantially to the interaction (Fig. 4c). Despite the similarity with NLRP3, NLRC4 uses only the corresponding FISNA loop 1 in oligomerization whereas FISNA loop 2 and the equivalent β-hairpin loop in WHD are barely present in NLRC4 (Extended Data Figs. 7d and 8d). In fact, very different interaction surfaces are used in the NLRP3 and NLRC4 discs; if one of the subunits in a pair of NLRP3 subunits is aligned to that in a pair of NLRC4 subunits, the neighbouring subunit in the NLRC4 pair needs to rotate by around 32° to match the orientation of that in the NLRP3 pair (Extended Data Fig. 8e).

To test the importance of NLRP3 interfacial residues on NLRP3 inflammasome activation, we generated charge reversal and alanine mutations on these residues (Fig. 4e). We then reconstituted wild-type (WT) and mutant human NLRP3 into NLRP3$^{-/-}$ mouse immortalized bone marrow-derived macrophages (iBMDMs) to examine the response following NLRP3 stimulation. We previously used this system successfully to examine the NLRP3–NEK7 interface in NLRP3 inflammasome activation[8]. Following priming by Toll-like receptor (TLR) ligand lipopolysaccharides (LPS) and stimulation by nigericin, WT NLRP3-reconstituted NLRP3$^{-/-}$ iBMDMs activated caspase-1, as shown by the appearance of the processed p20 band (Fig. 4e and Supplementary Fig. 1). FISNA domain mutants R147E, E152R, N155A, R157E, K166E and E176R, and HD1 and WHD mutants Q424A and Q509A, were strongly defective in caspase-1 processing. FISNA mutant D213R and NBD mutants Q359A and H364E were less or not impaired in caspase-1 processing (Fig. 4e). These data confirmed the functional role of the structurally observed interface in the NLRP3 inflammasome disc.

Discussion

The cryo-EM structures of the NLRP3–NEK7–ASC complex presented here provide structural characterization of the active NLRP3 inflammasome, and show important implications in the mechanism of NLRP3 activation and new ways to target NLRP3. First, from these NLRP3 structures we identified the mechanism of NLRP3 oligomerization in the active state. We found that the FISNA domain is a critical mediator of both NLRP3 conformational change and oligomerization, which is consistent with defective NLRP3 activation by our single-site, structure-guided mutations and with previously reported impaired NLRP3 activation by complete or partial deletions of the FISNA domain[13]. The

FISNA domain is absent in most NLRPs and much shortened in NLRC4 and NAIP5, indicating variable mechanisms in NLR oligomerization. This is despite the similar, though not identical, conformational change in NLRP3 in comparison with NLRC4. We further propose that NLRP3 conformational change requires both ATP (or dATP)[9] binding and the FISNA domain, probably because of the insufficiency of either alone, to compensate for the energetic cost of activation, which echoes the conclusion that both cytochrome c and dATP (or ATP) are required to fully activate the Apaf-1 apoptosome[44,48].

Second, the structures illuminate the role of LRR and NEK7 in NLRP3 inflammasome assembly. Surprisingly, we found that neither NEK7 nor LRR directly participates in NLRP3 oligomerization. What then are the functions of NEK7 and LRR? Together with the inactive cage structure of NLRP3 (refs. [9–11]), we propose that LRR and NEK7 are additional molecular switches in NLRP3 activation: whereas LRR is required for the inactive cage structure, its interaction with NEK7 at the MTOC disrupts the cage to allow formation of the active NLRP3 disc. Thus the NLRP3 inflammasome pathway may comprise the following steps: (1) priming by TLR ligands such as LPS to upregulate NLRP3 expression and prepare cells in other ways; (2) formation of NLRP3 cage on the TGN before stimulation; (3) NLRP3 conformational change and TGN dispersion following nigericin stimulation; (4) trafficking of dispersed TGN vesicles on microtubules to the MTOC; (5) opening of NLRP3 cage by the centrosome-resident protein NEK7 into two halves already tethered together, even if weakly, by a short PYD filament[9]; and (6) formation of the NLRP3 disc in the active conformation assisted by, and capable of, ASC recruitment (Fig. 5). Although we do not have direct evidence, the last step in the pathway may utilize the two half-cages generated on NEK7 binding, each comprising five subunits in the case of human NLRP3 (ref. [10]), to rearrange into an inflammasome disc. Thus, the unique NLRP3 pathway makes use of the already oligomeric cage to unfurl and convert into the active disc assembly, akin to a closed bud opening into a blooming flower.

Our active NLRP3 structures showed that NEK7 does not directly participate in NLRP3 oligomerization. In addition, unlike Apaf-1 or NAIP in which cytochrome c or flagellin binding overcomes autoinhibition[41,42,44], NEK7 binding is compatible with either inactive or active NLRP3 conformation and is thus unlikely to trigger NLRP3 activation. These observations help to rationalize how NLRP3 may be activated without NEK7 under certain conditions[49]; we hypothesize that these conditions may associate with higher NLRP3 expression or destabilization of the cage, to enable the inflammasome assembly from either caged or monomeric NLRP3 (Extended Data Fig. 9a). Our structures also suggest how LRR-deleted NLRP3, which cannot form the cage, may form an active inflammasome when overexpressed[50], probably also in an NEK7-independent manner (Extended Data Fig. 9b). More studies are required to dissect how NLRP3 senses multiple stimuli, and to explain other mechanistic details of the NLRP3 pathway to guide therapeutic intervention.

Methods

Plasmid construction

Full-length human NLRP3 and full-length human NEK7 were cloned into pTT3 vector with an N-terminal MBP tag and into pFLAG-CMV4 vector with an N-terminal FLAG

tag, respectively. Human ASC^{PYD} (residues 1–106) was cloned into pDB-His-MBP vector and expressed as an MBP fusion protein with an additional N-terminal 6× His tag as reported previously[18]. For reconstitution of WT and mutant NLRP3 into NLRP3$^{-/-}$ mouse bone marrow-derived macrophages (BMDMs), full-length human NLRP3 was cloned into an in-house-modified pLV-eGFP vector in which enhanced green fluorescent protein was replaced by mNG, as reported previously[8]. All constructs were confirmed by sequencing.

Protein expression and purification

Expi293F cells, maintained in 800 ml of Expi293 Expression Media (ThermoFisher), were fed with 6 m MKCl and grown to 2.0×10^6 cells ml^{-1}. These were transiently cotransfected with 0.5 mg of NLRP3 plasmid and 0.3 mg of NEK7 plasmid using 2.4 mg of polyethylenimine (Polysciences, Inc.). Cells were fed with 10 mM sodium butyrate and 8 ml of 45% d-(+) glucose solution at 12 h after transfection. Cells were harvested another 48 h later by 20 min centrifugation at 2,500 rpm. The collected cells were resuspended in PBS, treated for 30 min with 20 μM z-VAD-FMK, a pan-caspase inhibitor, and stimulated for a further 30 min with 10 μg ml^{-1} nigericin (13.4 μM). After stimulation, cells were lysed by sonication in the presence of a protease inhibitor cocktail (Roche) and centrifuged at 40,000 rpm for 1 h. The supernatant was collected and incubated with anti-FLAG resin for 1 h at 4 °C, with gentle rotation, and the resin washed with PBS. Bound proteins were eluted using PBS with the addition of 0.1 mg ml^{-1} FLAG peptide, and concentrated. His-MBP-ASC^{PYD} was expressed in *Escherichia coli* and purified by Ni-NTA affinity and gel filtration chromatography using a Superdex 200 column. To reconstitute the active NLRP3 inflammasome, 1 mM ATPγS, 2.5 mM MgCl$_2$ and either one- or tenfold molar excess ASC^{PYD} were added to the NLRP3–NEK7 complex, and MBP tags on NLRP3 and ASC^{PYD} were removed by incubation overnight with tobacco etch virus protease at 1:20 molar ratio. The molar concentration of ASC or the NLRP3–NEK7 complex was determined by optical density (OD$_{280}$) absorption, extinction coefficient and the molecular weight of His-MBP-ASC or the MBP–NLRP3–NEK7 complex. The mixture was applied to a Superose 6 gel filtration column equilibrated with running buffer (20 mM Tris pH 8.0, 150 mM NaCl and 1 mM tris(2-carboxyethyl)phosphine hydrochloride), and the peak near void was collected and concentrated to 0.8 mg ml^{-1} for EM experiments.

Negative-staining electron microscopy

Five microlitres of tenfold diluted NLRP3–NEK7–ASC complex was applied to a copper grid (Electron Microscopy Sciences, no. FCF400CU50), incubated for 1 min and absorbed with filter paper. The grid was then stained with 2% uranyl formate for 1 min and air-dried. Images were collected using a Tecnai G2 Spirit BioTWIN transmission electron microscope.

Cryo-EM grid preparation and data acquisition

Before grid preparation, 1 mM ATPγS and 2.5 mM MgCl$_2$ were added to the protein sample with incubation on ice for 1 h. A 3.5 μl drop containing the NLRP3–NEK7–ASC complex was loaded onto a glow-discharged Quantifoil grid (R1.2/1.3 400-mesh gold-supported holey carbon, Electron Microscopy Sciences), blotted for 3–4 s under 100% humidity at 4 °C and plunged into liquid ethane with Mark IV Vitrobot (ThermoFisher). Automated data collection was performed using SerialEM (Mastronarde, 2005), and videos were acquired

on a Titan Krios microscope (ThermoFisher) operating at 300 keV and equipped with a BioQuantum K3 Imaging Filter (Gatan, slit width 20 eV). Videos were recorded with a K3 Summit direct electron detector (Gatan) operating in super-resolution mode at ×81,000 magnification (0.53 Å per pixel). All videos were exposed at a total dose of 50.4 e $Å^{-2}$ over 40 frames with defocus range between −1.0 and −2.0 μm.

Cryo-EM data processing

All data-processing software support was acquired from the SBGrid Consortium. Overall, 11,356 videos were corrected by beam-induced motion using the Relion v.3.1 (ref. [51]) implementation of the Motion-Cor2 algorithm[52]. The contrast transfer function (CTF) and defocus estimation of micrographs were calculated by CTFFIND4 (ref. [53]). Images were imported into CryoSPARC[54] for further data processing. Two hundred images were selected and autopicked using the Blob Picker function in CryoSPARC, resulting in 95,296 particles. 2D classification was then used to generate templates for the Template Picker function in CryoSPARC, from which a total of 808,941 particles were picked. All particles were extracted with 8× binning (4.24 Å pixel size) at a box size of 128 pixels, then subjected to reference-free 2D classification. Bad particles were rejected, and good 2D classes with clear top or side views were selected. After rounds of 2D classification, 322,527 particles were selected and extracted with 2× binning at a box size of 512 pixels. The resulting particles were applied for ab initio reconstruction with $K = 5$, followed by heterogeneous refinement. Further reference-free 2D classification of particles from the two best three-dimensional classes was performed, resulting in three final datasets corresponding to 140,634 incomplete discs with four blades, 51,576 10-fold discs and 31,004 11-fold discs. Ab initio reconstruction and homogeneous refinement were conducted for each dataset without applying symmetry, which resulted in a 4.38 Å map for the tenfold disc and a 5.12 Å map for the 11-fold disc; for incomplete discs nonuniform refinement was further performed, resulting in a 3.82 Å map. For the 10- and 11-fold discs, C10 and C11 symmetry were applied during nonuniform refinement, leading to 3.49 and 3.89 Å maps, respectively. After local CTF refinement and local masked refinement, maps for the 10- and 11-fold discs were improved to 3.40 and 3.79 Å resolution, respectively.

PYD filament reconstruction

We selected 43,255 particles containing stacked discs with short filaments in the middle from the initial 2D classification and re-extracted with 2× binning at a box size of 200 pixels. After further 2D classification, 33,227 particles were selected for ab initio reconstruction without helical symmetry, and then for helical reconstruction starting from the helical parameter in previously solved PYD filament structures[18,55] (C3 symmetry, 54° in twist and 14 Å in rise per subunit). Two rounds of helical refinement converged at refined twist of 54.926° and rise of 14.320 Å, resulting in a 3.3 Å map of the NLRP3 PYD filament.

Model building and structure representation

The cryo-EM maps were first fit with the NLRP3–NEK7 complex structure[8] (PDB: 6NPY), NEK7 structure[37] (2WQM) and an AlphaFold predicted model[56] using UCSF Chimera[57] or ChimeraX[58], followed by manual adjustment in Coot[59] and real-space refinement in

Phenix[60]. For all structures we used PISA5 (ref. [47]) to analyse interactions. Structure representations were generated in ChimeraX[58] and Pymol[61].

Generation of stable cell lines

We used lentiviruses to reconstitute NLRP3$^{-/-}$ mouse iBMDMs with WT or mutant full-length mNG-tagged human NLRP3 following a previously described protocol[8], with the following modification. After spinfection to infect NLRP3$^{-/-}$ mouse iBMDMs with lentiviruses, cells were incubated for the expression of reconstituted proteins for 48 h and sorted on either a BD FACSAria Fusion or a FACSAria II cell sorter using a 100 μm nozzle at 20 psi. Sorted populations were gated to exclude dead and nonfluorescent cells.

Immunoblotting of whole-cell lysates

Wild-type iBMDMs, NLRP3$^{-/-}$ iBMDMs and NLRP3$^{-/-}$ iBMDMs reconstituted with mNG-tagged NLRP3 WT and mutants were seeded at 1×10^6 cells per well on a six-well tissue culture plate. The following day, cells were treated with 1 μg ml^{-1} LPS (Invivogen, no. tlrl-b5lps) for 4 h followed by NLRP3 activation with 20 μM nigericin (Sigma-Aldrich, no. N7143–5MG) for 1 h. Medium was discarded and the whole-cell lysate was prepared by the addition of 100 μl lysis buffer (150 mM NaCl, 50 mM Tris-HCl pH 7.5, 1% NP-40 and 5% glycerol) to each well. After 30 min, lysates were centrifuged for 10 min at 15,000 rpm to remove the pellets and SDS sample buffer was added, followed by loading onto a 4–12% Bis-Tris PAGE gel (Invitrogen, no. NP0336BOX) along with a Page Ruler Preset Ladder (Thermo Scientific, no. 26616). NLRP3, β-actin and the cleaved caspase-1 p20 fragment were visualized by immunoblotting using mouse primary antibodies anti-NLRP3 (1:2,000; Adipogen, no. AG-20B-0014-C100), mouse anti-β-actin (1:2,000; Sigma-Aldrich, no. A2228–100UL) and rabbit anti-p20 of caspase-1 (1:1,000; Cell Signaling, no. 89332S), respectively. Secondary antibodies used were anti-mouse-HRP (1:5,000; Cell Signaling, no. 7076S) and anti-rabbit-HRP (1:2,500; Cell Signaling, no. 7074S).

Reporting summary

Further information on research design is available in the Nature Portfolio Reporting Summary linked to this article.

Data availability

Atomic coordinates of the tenfold NLRP3–NEK7 assembly structure and NLRP3 PYD filament have been deposited in PDB under accession nos. 8EJ4 and 8ERT, respectively. Corresponding cryo-EM density maps have been deposited in the Electron Microscopy Data Bank under accession nos. EMD-28175 and EMD-28560, respectively. All other data are available from the corresponding authors on reasonable request.
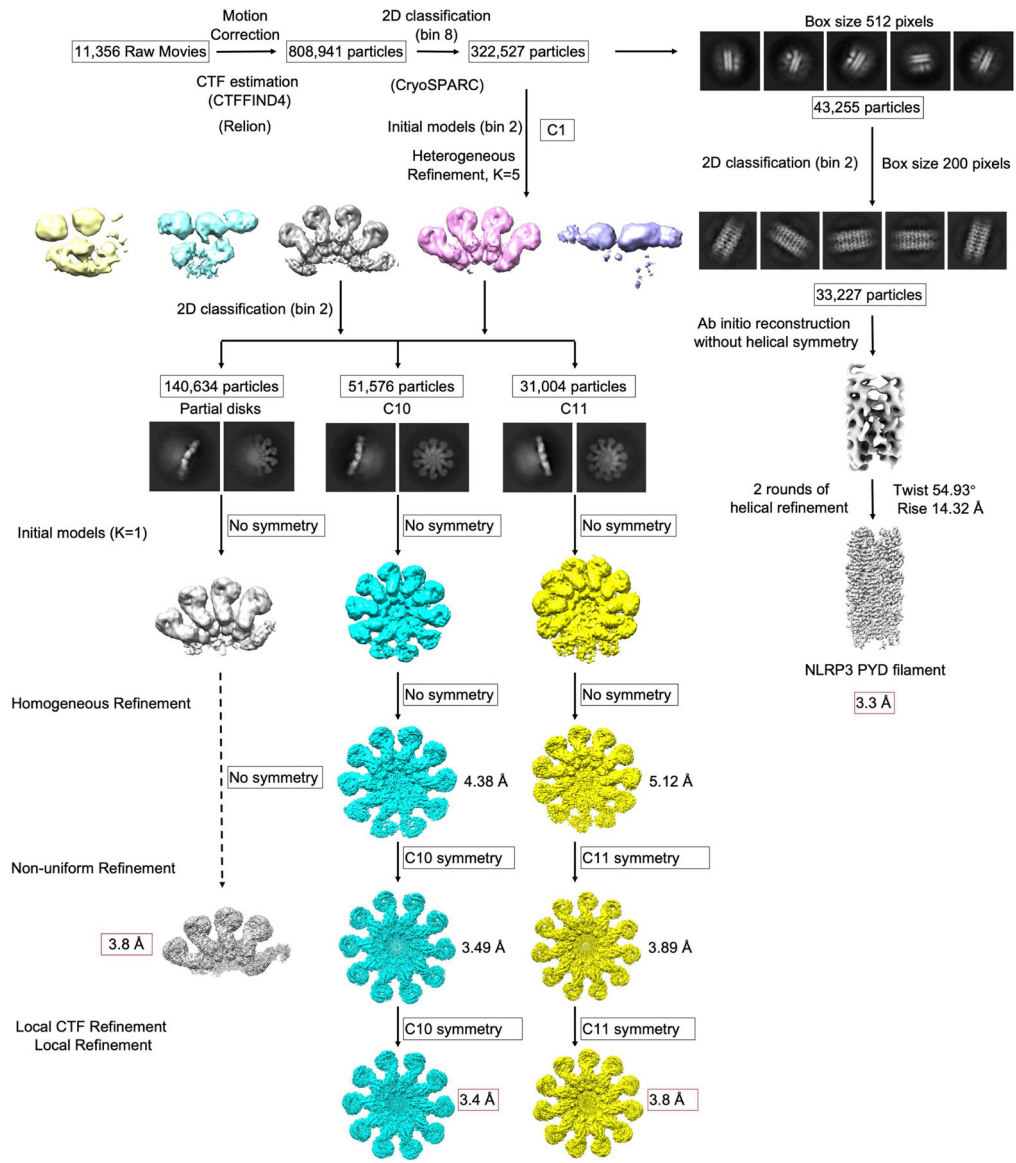
Extended Data
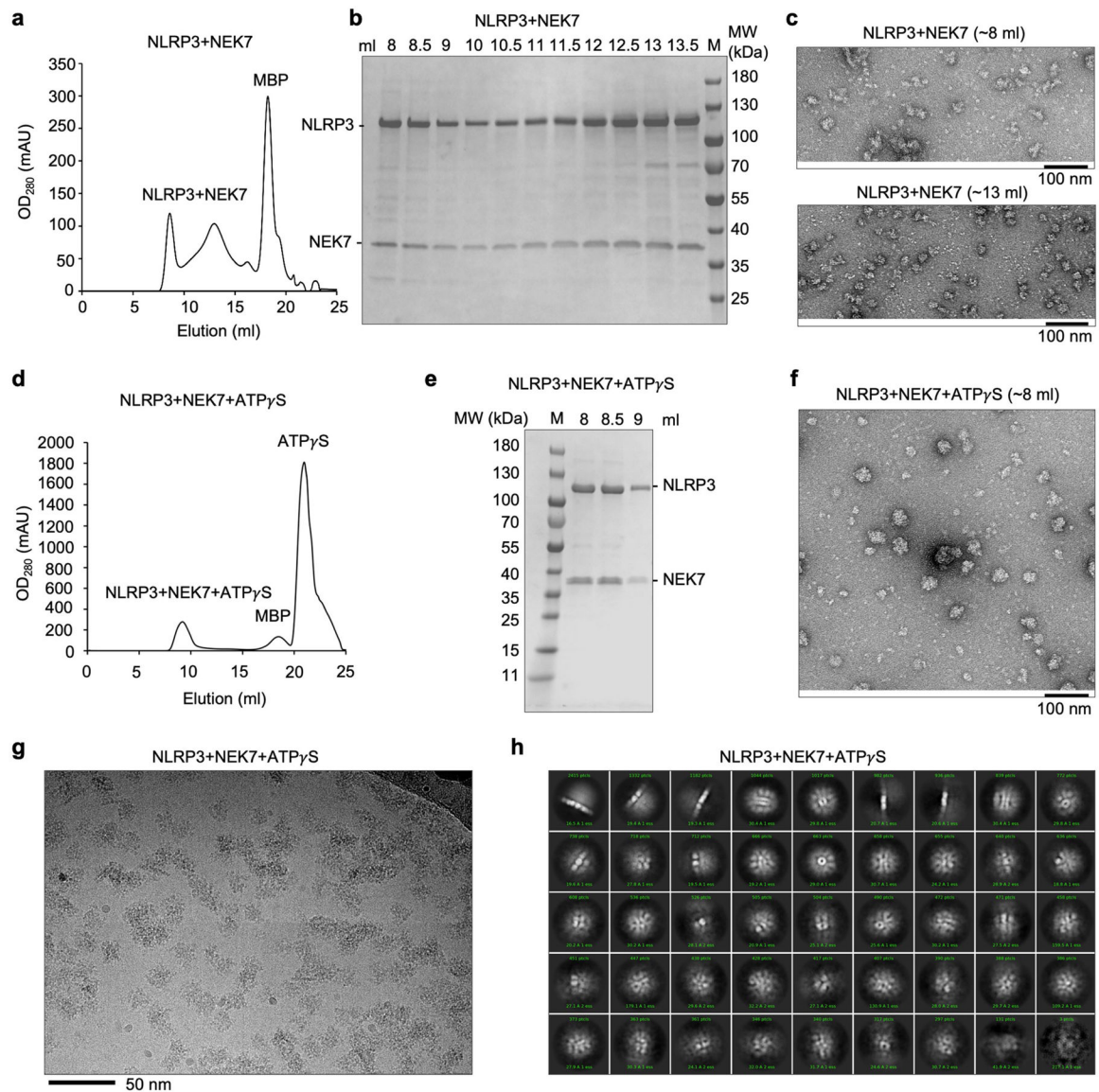
Extended Data Fig. 1 |. Preparation and characterization of the NLRP3-NEK7 complex.
a, Gel filtration profile of the NLRP3-NEK7 complex showing the two peaks. **b**, SDS-polyacrylamide gel electrophoresis (PAGE) of gel filtration fractions for the NLRP3-NEK7 complex. Locations of the two component proteins are labeled. **c**, Representative negative-staining images from the two NLRP3-NEK7 complex peaks. **d**, Gel filtration profile of the NLRP3-NEK7 complex with ATPγS showing one major peak. **e**, SDS-PAGE of the gel filtration fractions for the NLRP3-NEK7 complex with ATPγS. Locations of the two component proteins are labeled. **f**, A representative negative-staining image from the peak containing NLRP3, NEK7 and ATPγS. **g**, A representative cryo-EM image from the peak containing NLRP3, NEK7 and ATPγS. Experiments in (a-g) were repeated at least three times. **h**, 2D classes from cryo-EM images of the NLRP3-NEK7 complex with ATPγS. No full disk was observed.
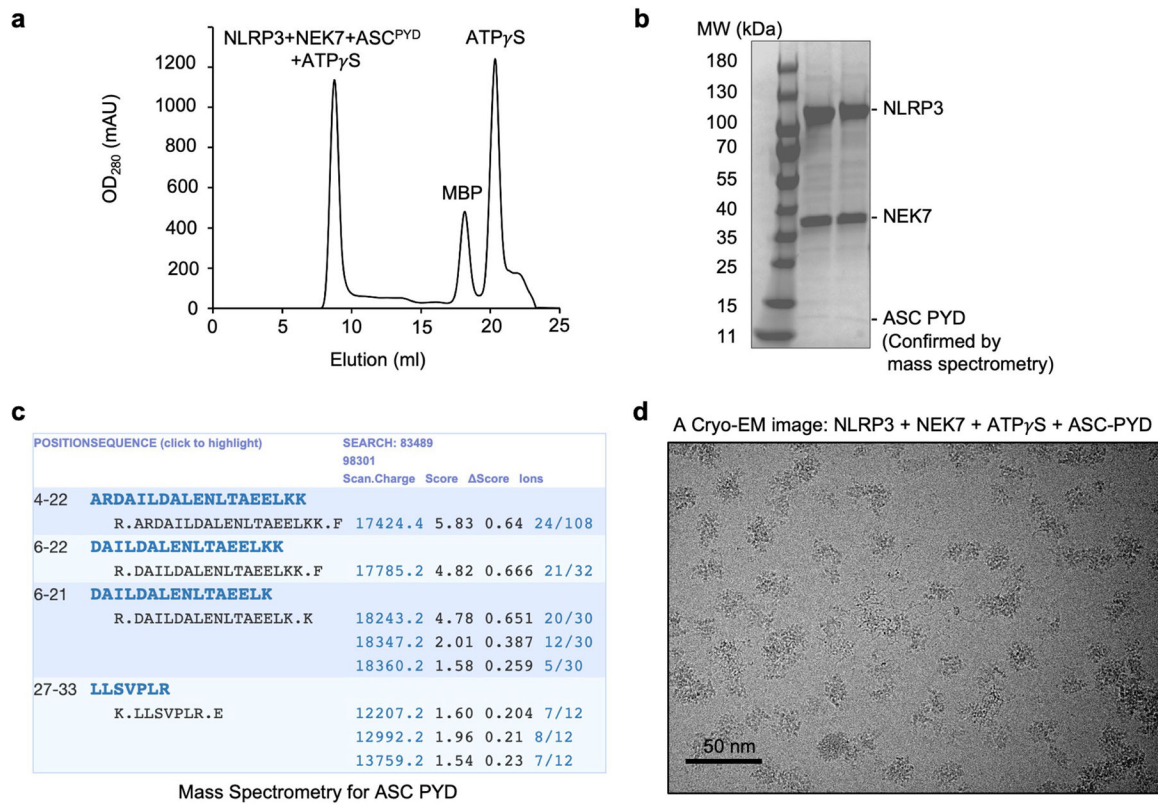
Extended Data Fig. 2 |. Preparation and characterization of NLRP3-NEK7-ASC inflammasome complexes.

a, Gel filtration profile of the NLRP3-NEK7-ASC complex. **b**, SDS- PAGE of the near void peak from the gel filtration chromatography. Locations of the three component proteins are labelled. **c**, Mass spectrometry that detected ASC PYD in the band in (b). **d**, A representative cryo-EM image from a sample containing NLRP3, NEK7, ATPγS, and 1:1 ASC PYD. Experiments in (a-b) and (d) were repeated at least three times.

Extended Data Fig. 3 |. Flow chart for cryo-EM data processing of the NLRP3-NEK7-ASC inflammasome complex.
Data processing details can be found in Methods.
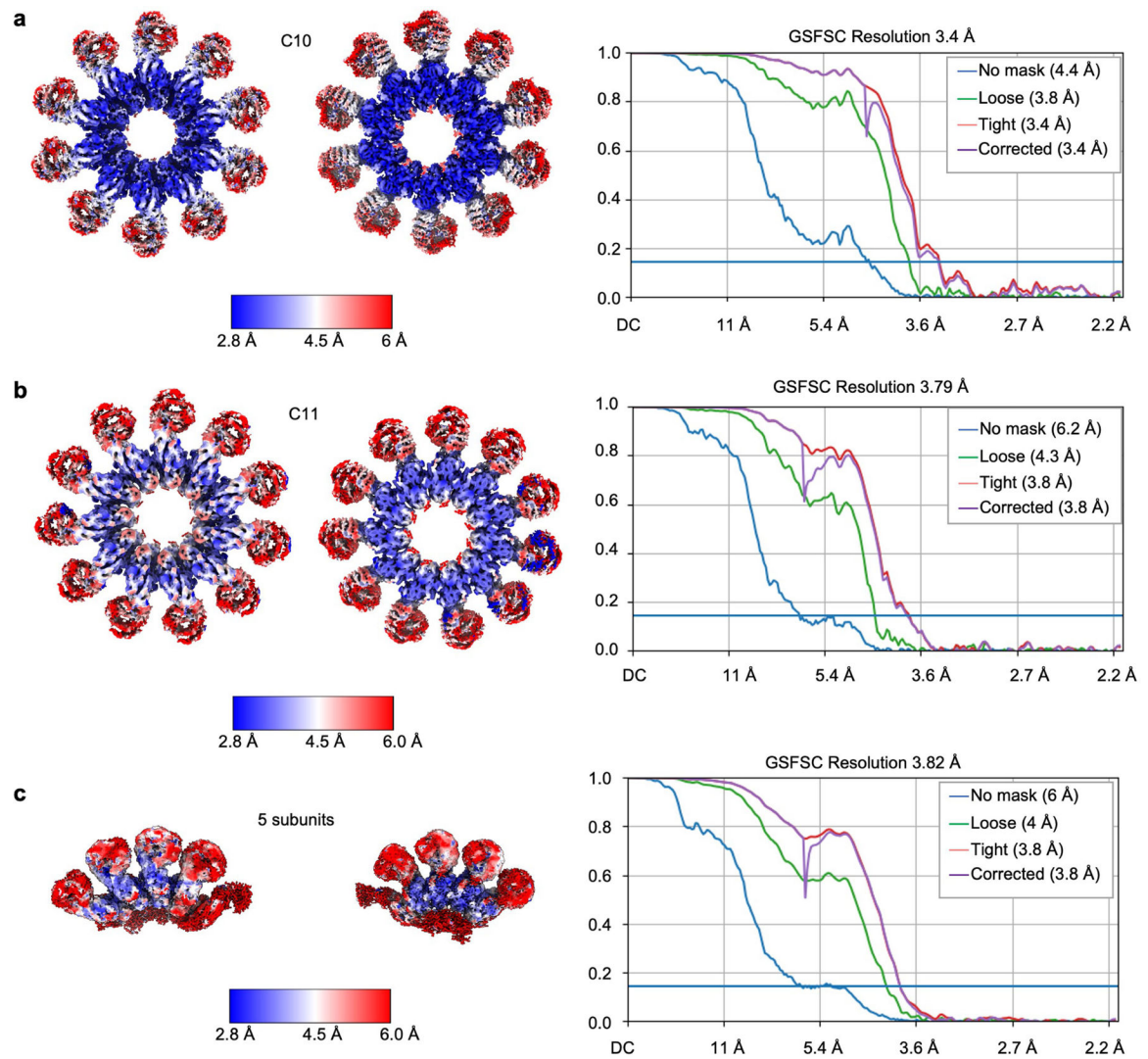
Extended Data Fig. 4 |. Local resolution distributions and Fourier shell correlation (FSC) curves.
a-c, The C10 NLRP3-NEK7-ASC complex (a), the C11 NLRP3-NEK7-ASC complex (b), and the partial NLRP3-NEK7 disk containing primarily 5 subunits (c).
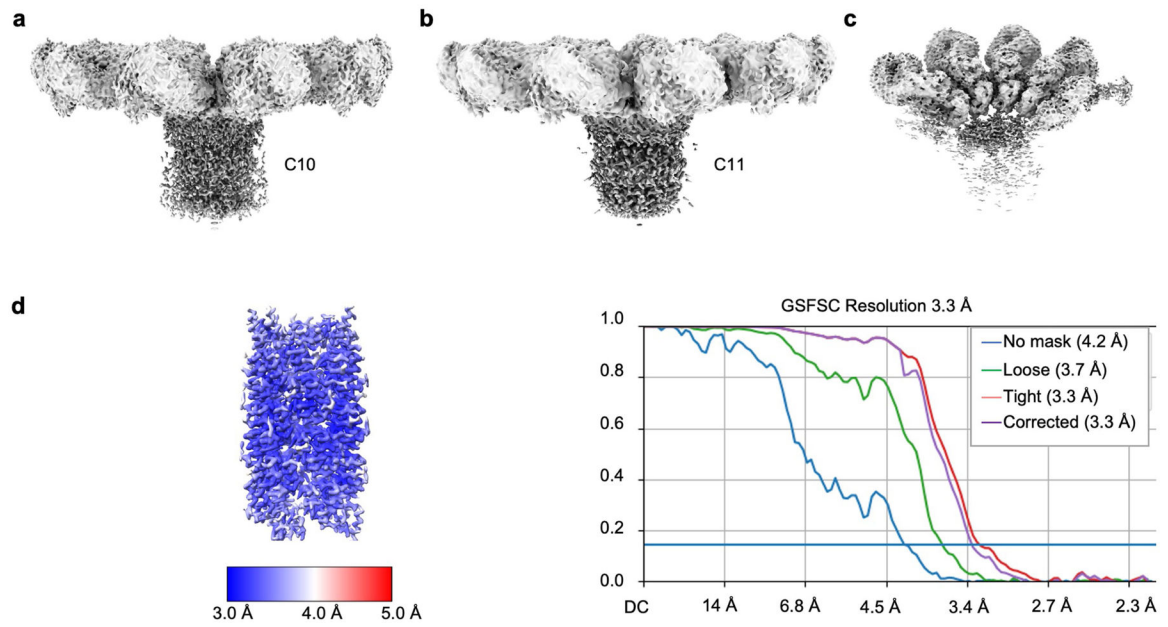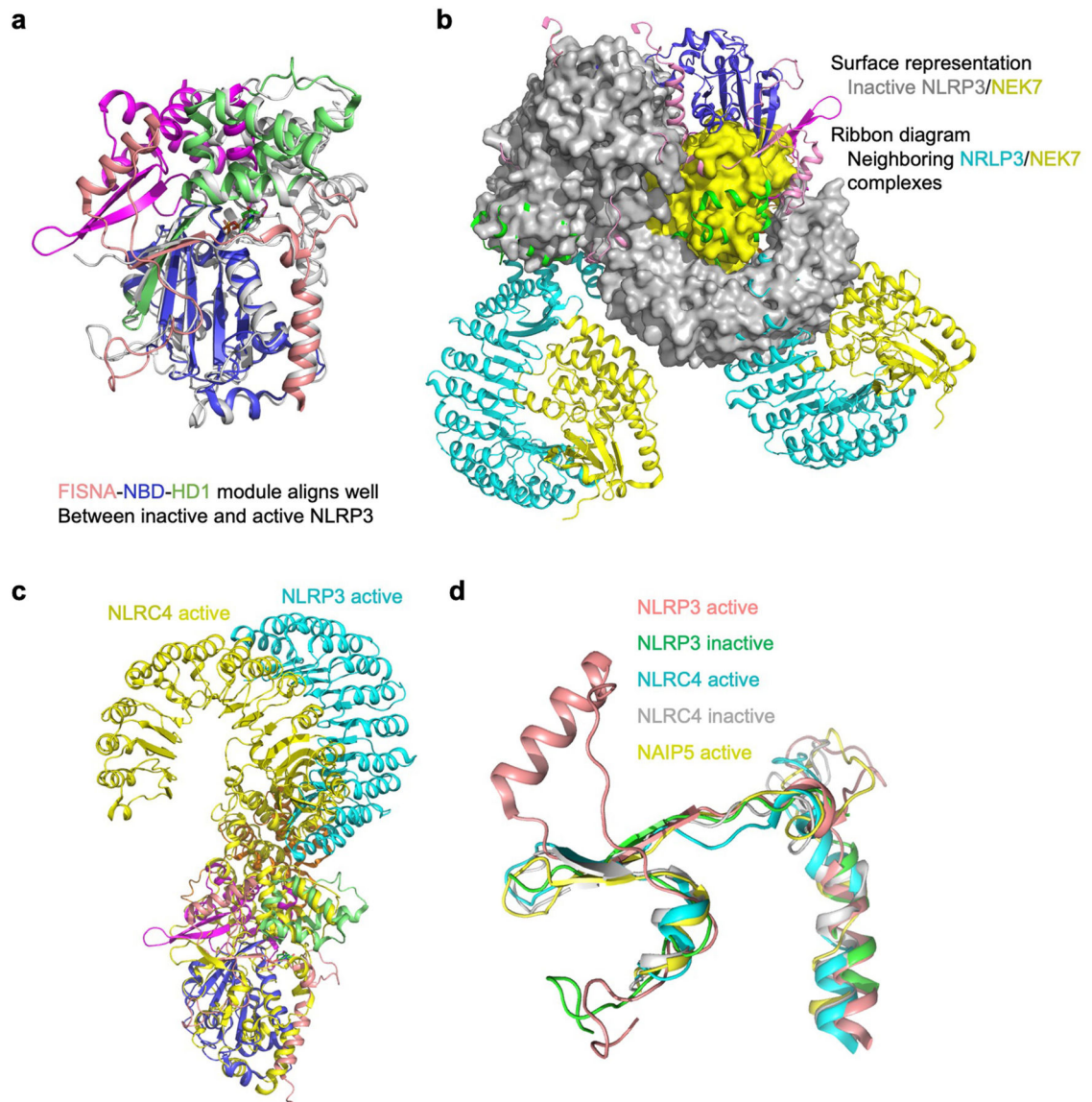
Extended Data Fig. 5 |. PYD helical filament.
a-c, Side views of the cryo-EM maps of the C10 NLRP3-NEK7-ASC complex (a), the C11 NLRP3-NEK7-ASC complex (b) and the partial disk of the NLRP3-NEK7 complex (c). **d**, Local resolution distribution and Fourier shell correlation (FSC) curve of the NLRP3 PYD filament.
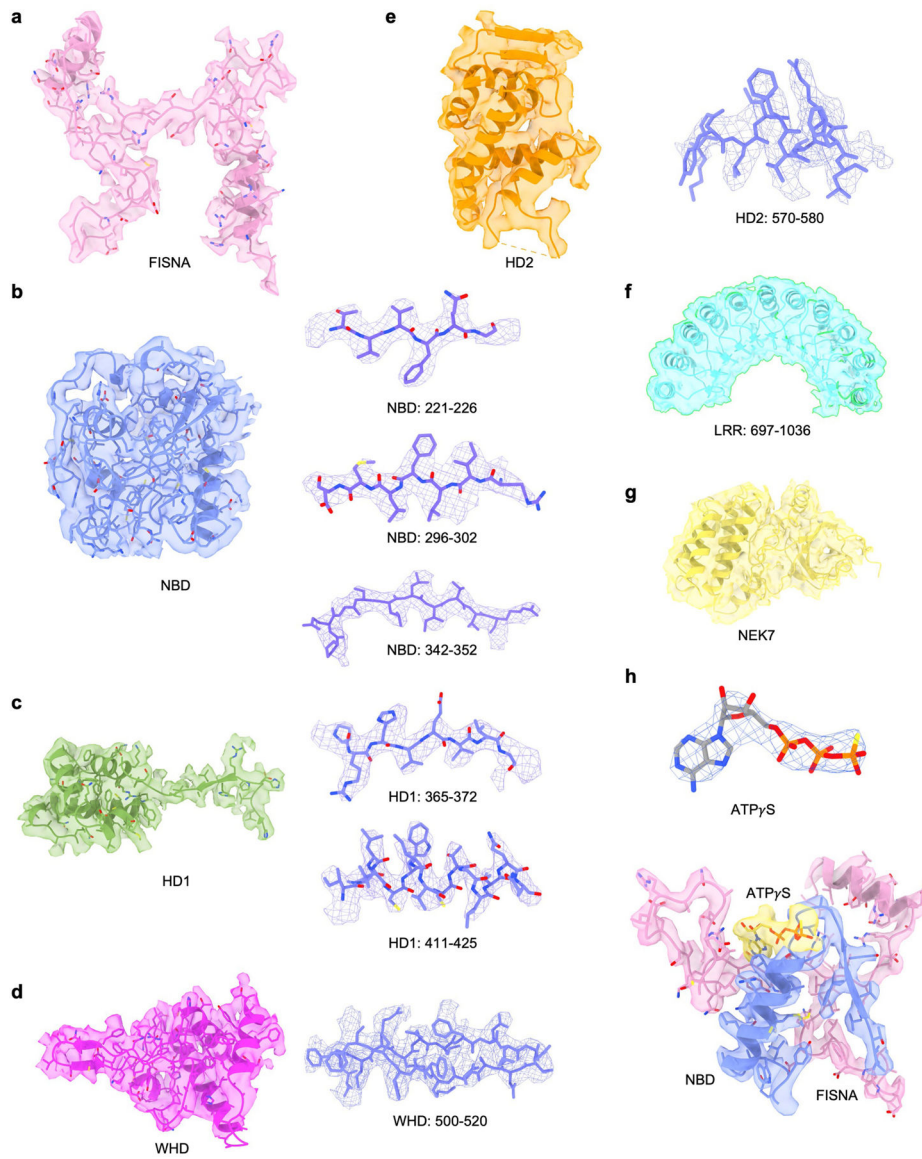
Extended Data Fig. 6 |. Close-up evaluation of the C10 NLRP3-NEK7-ASC complex map quality.
a-h, Cryo-EM maps in individual regions (labelled) superimposed with the final model.

a, FISNA-NBD-HD1 module aligns well Between inactive and active NLRP3

b, Surface representation Inactive NLRP3/NEK7

Ribbon diagram Neighboring NRLP3/NEK7 complexes

c, NLRC4 active   NLRP3 active

d, NLRP3 active
NLRP3 inactive
NLRC4 active
NLRC4 inactive
NAIP5 active

Extended Data Fig. 7 |. Conformational change and comparison with NLRC4.
a, Superposition of active NLRP3 (in domain colours) and inactive NLRP3 (PDB: 6NPY in grey) by the FISNA-NBD-HD1 domain. The WHD domain of inactive NLRP3 situates behind the superimposed HD1, different from that of active NLRP3. **b**, Superposition of active NLRP3 and inactive NLRP3 (PDB: 6NPY in grey), showing the LRR domain and NEK7 of the inactive NLRP3-NEK7 complex would have been in clash with a neighbouring NLRP3 molecule. **c**, Superposition of active NLRP3 with active NLRC4 (PDB: 3JBL in yellow) by the FISNA-NBD-HD1 domain. **d**, Superposition of the FISNA domain from active NLRP3 (salmon), inactive NLRP3 (PDB: 6NPY in green), active NLRC4 (PDB: 3JBL in cyan), inactive NLRC4 (PDB: 4KXF in grey), and active NAIP5 (6B5B in yellow).
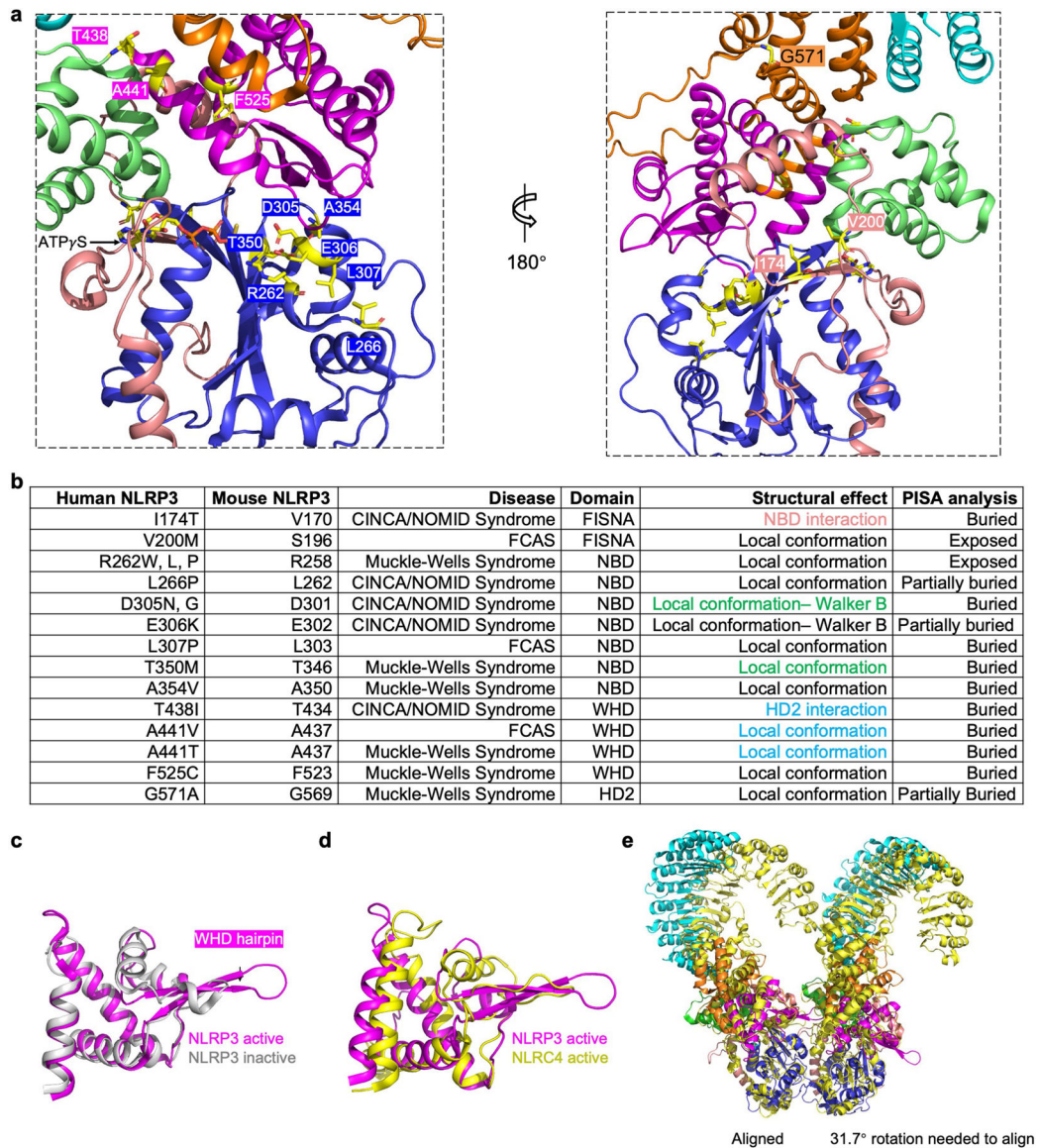
Extended Data Fig. 8 |. Mapping of the CAPS mutations on active NLRP3, and comparison of active NLRP3 and NLRC4.

a, Locations of CAPS mutation sites on the active NLRP3 structure. Two views are shown. **b**, A list of the mutations, their domain location and potential structural effects. **c**, Superposition of the WHD from active NLRP3 (magenta) and inactive NLRP3 (PDB: 6NPY in grey), showing the formation of a β-hairpin in the active state. **d**, Superposition of the WHD from active NLRP3 (magenta) and active NLRC4 (PDB: 3JBL in yellow), showing lack of the β-hairpin in NLRC4. **e**, Superposition of one NLRP3 subunit in two neighbouring NLRP3 subunits in a disk (coloured by domains) with one NLRC4 subunit in two neighbouring NLRC4 subunits in a disk (PDB: 3JBL in yellow). The second NLRC4 subunit needs to rotate by 31.7° to align with the second NLRP3 subunit.
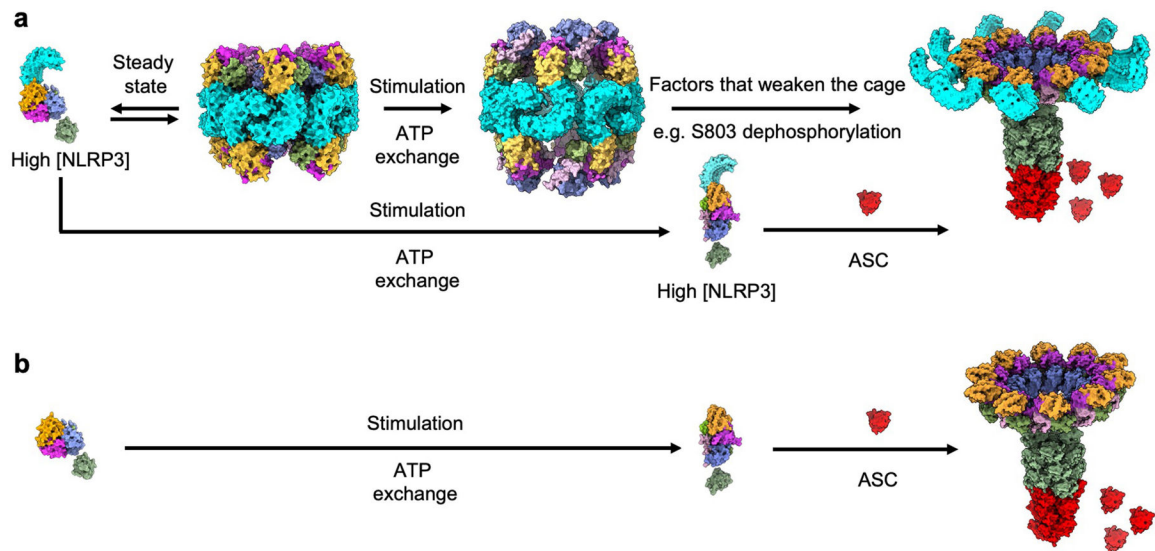
Extended Data Fig. 9 |. A structure-derived model for potential NEK7-independent, and LRR-deleted NLRP3 inflammasome activation.

a, Under certain conditions such as those marked in the schematic (e.g. high NLRP3 expression level or certain effects from priming), monomeric NLRP3 or destabilized caged NLRP3 may directly form the active NLRP3 disk with ASC upon stimulation. **b**, For overexpressed LRR-deleted NLRP3, stimulation would likely directly induce the activating conformational change to allow the assembly of the inflammasome disk with ASC.

Supplementary Material

Refer to Web version on PubMed Central for supplementary material.

Acknowledgments

References

1. Wang L, Sharif H, Vora SM, Zheng Y & Wu H Structures and functions of the inflammasome engine. J. Allergy Clin. Immunol 147, 2021–2029 (2021). [PubMed: 34092352]

2. Swanson KV, Deng M & Ting JP-Y The NLRP3 inflammasome: molecular activation and regulation to therapeutics. Nat. Rev. Immunol 19, 477–489 (2019). [PubMed: 31036962]

3. Gaidt MM & Hornung V The NLRP3 inflammasome renders cell death pro-inflammatory. J. Mol. Biol 430, 133–141 (2018). [PubMed: 29203171]

4. Nozaki K, Li L & Miao EA Innate sensors trigger regulated cell death to combat intracellular infection. Annu. Rev. Immunol 40, 469–498 (2022). [PubMed: 35138947]

5. Deets KA & Vance RE Inflammasomes and adaptive immune responses. Nat. Immunol 22, 412–422 (2021). [PubMed: 33603227]

6. Coll RC et al. MCC950 directly targets the NLRP3 ATP-hydrolysis motif for inflammasome inhibition. Nat. Chem. Biol 15, 556–559 (2019). [PubMed: 31086327]

7. Tapia-Abellán A et al. MCC950 closes the active conformation of NLRP3 to an inactive state. Nat. Chem. Biol 15, 560–564 (2019). [PubMed: 31086329]

8. Sharif H et al. Structural mechanism for NEK7-licensed activation of NLRP3 inflammasome. Nature 570, 338–343 (2019). [PubMed: 31189953]

9. Andreeva L et al. NLRP3 cages revealed by full-length mouse NLRP3 structure control pathway activation. Cell 184, 6299–6312.e22 (2021). [PubMed: 34861190]

10. Hochheiser IV et al. Structure of the NLRP3 decamer bound to the cytokine release inhibitor CRID3. Nature 604, 184–189 (2022). [PubMed: 35114687]

11. Ohto U et al. Structural basis for the oligomerization-mediated regulation of NLRP3 inflammasome activation. Proc. Natl Acad. Sci. USA 119, e2121353119 (2022). [PubMed: 35254907]

12. Dekker C et al. Crystal structure of NLRP3 NACHT domain with an inhibitor defines mechanism of inflammasome inhibition. J. Mol. Biol 433, 167309 (2021). [PubMed: 34687713]

13. Tapia-Abellán A et al. Sensing low intracellular potassium by NLRP3 results in a stable open structure that promotes inflammasome activation. Sci. Adv 7, eabf4468 (2021). [PubMed: 34524838]

14. Muñoz-Planillo R et al. K^+ efflux is the common trigger of NLRP3 inflammasome activation by bacterial toxins and particulate matter. Immunity 38, 1142–1153 (2013). [PubMed: 23809161]

15. Magupalli VG et al. HDAC6 mediates an aggresome-like mechanism for NLRP3 and pyrin inflammasome activation. Science 369, eaas8995 (2020). [PubMed: 32943500]

16. Chen J & Chen ZJ PtdIns4P on dispersed trans-Golgi network mediates NLRP3 inflammasome activation. Nature 564, 71–76 (2018). [PubMed: 30487600]

17. Li X et al. MARK4 regulates NLRP3 positioning and inflammasome activation through a microtubule-dependent mechanism. Nat. Commun 8, 15986 (2017). [PubMed: 28656979]

18. Lu A et al. Unified polymerization mechanism for the assembly of ASC-dependent inflammasomes. Cell 156, 1193–1206 (2014). [PubMed: 24630722]

19. Hochheiser IV et al. Directionality of PYD filament growth determined by the transition of NLRP3 nucleation seeds to ASC elongation. Sci. Adv 8, eabn7583 (2022). [PubMed: 35559676]

20. Li Y et al. Cryo-EM structures of ASC and NLRC4 CARD filaments reveal a unified mechanism of nucleation and activation of caspase-1. Proc. Natl Acad. Sci. USA 115, 10845–10852 (2018). [PubMed: 30279182]

21. Lu A et al. Molecular basis of caspase-1 polymerization and its inhibition by a new capping mechanism. Nat. Struct. Mol. Biol 23, 416–425 (2016). [PubMed: 27043298]

22. He Y, Zeng MY, Yang D, Motro B & Núñez G NEK7 is an essential mediator of NLRP3 activation downstream of potassium efflux. Nature 530, 354–357 (2016). [PubMed: 26814970]

23. Schmid-Burgk JL et al. A genome-wide CRISPR (clustered regularly interspaced short palindromic repeats) screen identifies NEK7 as an essential component of NLRP3 inflammasome activation. J. Biol. Chem 291, 103–109 (2016). [PubMed: 26553871]

24. Shi H et al. NLRP3 activation and mitosis are mutually exclusive events coordinated by NEK7, a new inflammasome component. Nat. Immunol 17, 250–258 (2016). [PubMed: 26642356]

25. Martinon F, Burns K & Tschopp J The inflammasome: a molecular platform triggering activation of inflammatory caspases and processing of proIL-β. Mol. Cell 10, 417–426 (2002). [PubMed: 12191486]

26. Ding J et al. Pore-forming activity and structural autoinhibition of the gasdermin family. Nature 535, 111–116 (2016). [PubMed: 27281216]

27. Liu X et al. Inflammasome-activated gasdermin D causes pyroptosis by forming membrane pores. Nature 535, 153–158 (2016). [PubMed: 27383986]

28. He W-t et al. Gasdermin D is an executor of pyroptosis and required for interleukin-1β secretion. Cell Res 25, 1285–1298 (2015). [PubMed: 26611636]

29. Kayagaki N et al. Caspase-11 cleaves gasdermin D for non-canonical inflammasome signalling. Nature 526, 666–671 (2015). [PubMed: 26375259]

30. Shi J et al. Cleavage of GSDMD by inflammatory caspases determines pyroptotic cell death. Nature 526, 660–665 (2015). [PubMed: 26375003]

31. Lieberman J, Wu H & Kagan JC Gasdermin D activity in inflammation and host defense. Sci. Immunol 4, eaav1447 (2019). [PubMed: 31492708]

32. Gaidt MM & Hornung V Pore formation by GSDMD is the effector mechanism of pyroptosis. EMBO J 35, 2167–2169 (2016). [PubMed: 27572465]

33. Booshehri LM & Hoffman HM Caps and NLRP3. J. Clin. Immunol 39, 277–286 (2019). [PubMed: 31077002]

34. Touitou I et al. Infevers: an evolving mutation database for auto-inflammatory syndromes. Hum. Mutat 24, 194–198 (2004). [PubMed: 15300846]

35. Mangan MS et al. Targeting the NLRP3 inflammasome in inflammatory diseases. Nat. Rev. Drug Discov 17, 588–606 (2018). [PubMed: 30026524]

36. Duncan JA et al. Cryopyrin/NALP3 binds ATP/dATP, is an ATPase, and requires ATP binding to mediate inflammatory signaling. Proc. Natl Acad. Sci. USA 104, 8041–8046 (2007). [PubMed: 17483456]

37. Richards MW et al. An autoinhibitory tyrosine motif in the cell-cycle-regulated Nek7 kinase is released through binding of Nek9. Mol. Cell 36, 560–570 (2009). [PubMed: 19941817]

38. Zhang L et al. Cryo-EM structure of the activated NAIP2-NLRC4 inflammasome reveals nucleated polymerization. Science 350, 404–409 (2015). [PubMed: 26449474]

39. Hu Z et al. Structural and biochemical basis for induced self-propagation of NLRC4. Science 350, 399–404 (2015). [PubMed: 26449475]

40. Hu Z et al. Crystal structure of NLRC4 reveals its autoinhibition mechanism. Science 341, 172–175 (2013). [PubMed: 23765277]

41. Tenthorey JL et al. The structural basis of flagellin detection by NAIP5: a strategy to limit pathogen immune evasion. Science 358, 888–893 (2017). [PubMed: 29146805]

42. Yang X et al. Structural basis for specific flagellin recognition by the NLR protein NAIP5. Cell Res 28, 35–47 (2018). [PubMed: 29182158]

43. Sandall CF, Ziehr BK & MacDonald JA ATP-binding and hydrolysis in inflammasome activation. Molecules 25, 4572 (2020). [PubMed: 33036374]

44. Zhou M et al. Atomic structure of the apoptosome: mechanism of cytochrome c-and dATP-mediated activation of Apaf-1. Genes Dev 29, 2349–2361 (2015). [PubMed: 26543158]

45. Yan N et al. Structure of the CED-4–CED-9 complex provides insights into programmed cell death in *Caenorhabditis elegans*. Nature 437, 831–837 (2005). [PubMed: 16208361]

46. Qi S et al. Crystal structure of the *Caenorhabditis elegans* apoptosome reveals an octameric assembly of CED-4. Cell 141, 446–457 (2010). [PubMed: 20434985]

47. Krissinel E & Henrick K Inference of macromolecular assemblies from crystalline state. J. Mol. Biol 372, 774–797 (2007). [PubMed: 17681537]

48. Li P et al. Cytochrome c and dATP-dependent formation of Apaf-1/caspase-9 complex initiates an apoptotic protease cascade. Cell 91, 479–489 (1997). [PubMed: 9390557]

49. Schmacke NA et al. IKKbeta primes inflammasome formation by recruiting NLRP3 to the trans-Golgi network. Immunity 10.1016/j.immuni.2022.10.021 (2022).

50. Hafner-Bratkovi I et al. NLRP3 lacking the leucine-rich repeat domain can be fully activated via the canonical inflammasome pathway. Nat. Commun 9, 5182 (2018). [PubMed: 30518920]

51. Zivanov J et al. New tools for automated high-resolution cryo-EM structure determination in RELION-3. eLife 7, e42166 (2018). [PubMed: 30412051]

52. Zheng SQ et al. MotionCor2: anisotropic correction of beam-induced motion for improved cryo-electron microscopy. Nat. Methods 14, 331–332 (2017). [PubMed: 28250466]

53. Rohou A & Grigorieff N CTFFIND4: fast and accurate defocus estimation from electron micrographs. J. Struct. Biol 192, 216–221 (2015). [PubMed: 26278980]

54. Punjani A, Rubinstein JL, Fleet DJ & Brubaker MA cryoSPARC: algorithms for rapid unsupervised cryo-EM structure determination. Nat. Methods 14, 290–296 (2017). [PubMed: 28165473]

55. Shen C et al. Molecular mechanism for NLRP6 inflammasome assembly and activation. Proc. Natl Acad. Sci. USA 116, 2052–2057 (2019). [PubMed: 30674671]

56. Tunyasuvunakool K et al. Highly accurate protein structure prediction for the human proteome. Nature 596, 590–596 (2021). [PubMed: 34293799]

57. Goddard TD, Huang CC & Ferrin TE Visualizing density maps with UCSF Chimera. J. Struct. Biol 157, 281–287 (2007). [PubMed: 16963278]

58. Goddard TD et al. UCSF ChimeraX: meeting modern challenges in visualization and analysis. Protein Sci 27, 14–25 (2018). [PubMed: 28710774]

59. Emsley P, Lohkamp B, Scott WG & Cowtan K Features and development of Coot. Acta Crystallogr. D Biol. Crystallogr 66, 486–501 (2010). [PubMed: 20383002]

60. Adams PD et al. PHENIX: a comprehensive Python-based system for macromolecular structure solution. Acta Crystallogr. D Biol. Crystallogr 66, 213–221 (2010). [PubMed: 20124702]

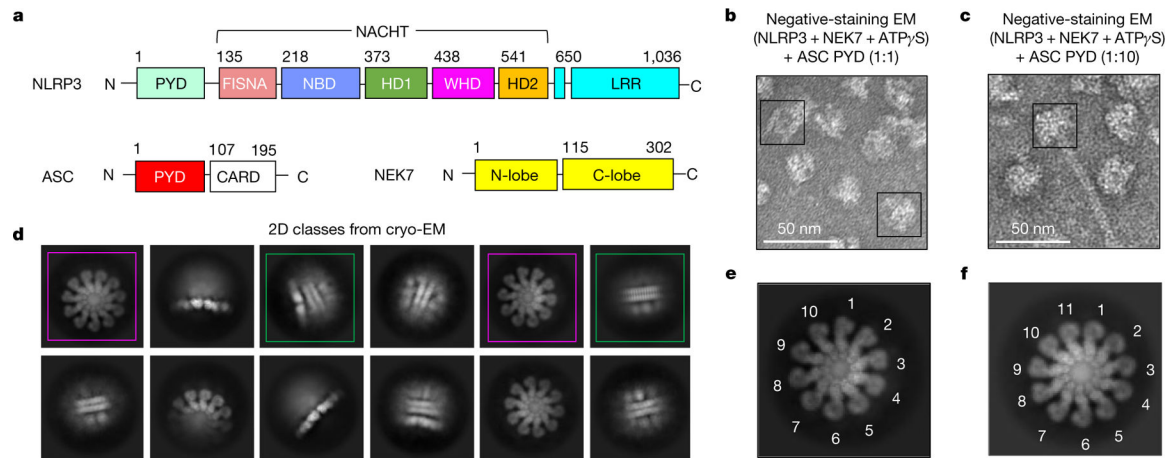61. DeLano WL Pymol: an open-source molecular graphics tool. CCP4 Newsl. Protein Crystallogr 40, 82–92 (2002).

Fig. 1 |. Preparation and characterization of the NLRP3–NEK7–ASC inflammasome complex.
a, Domain organizations of human NLRP3, NEK7 and ASC. Approximate domain boundaries are labelled. **b**, Representative negative-staining EM image from a purified sample containing NLRP3, NEK7, ATPγS and 1:1 ASC PYD. A stacked NLRP3–NEK7 complex (left) and a single NLRP3–NEK7–ASC complex (right) are enclosed by two black squares. **c**, Representative negative-staining EM image from a purified sample similar to that in **b** but containing tenfold excess ASC PYD. An NLRP3–NEK7–ASC complex with a long ASC filament is indicated by the black square. **b,c**, Experiments were repeated at least three times. **d**, 2D classes from cryo-EM images of the sample in **b**. Magenta squares indicate examples of top/bottom views of complete discs, and green squares highlight the central NLRP3 PYD filament from stacked discs. **e,f**, Enlarged views of tenfold (**e**) and 11-fold (**f**) 2D classes from **d**.
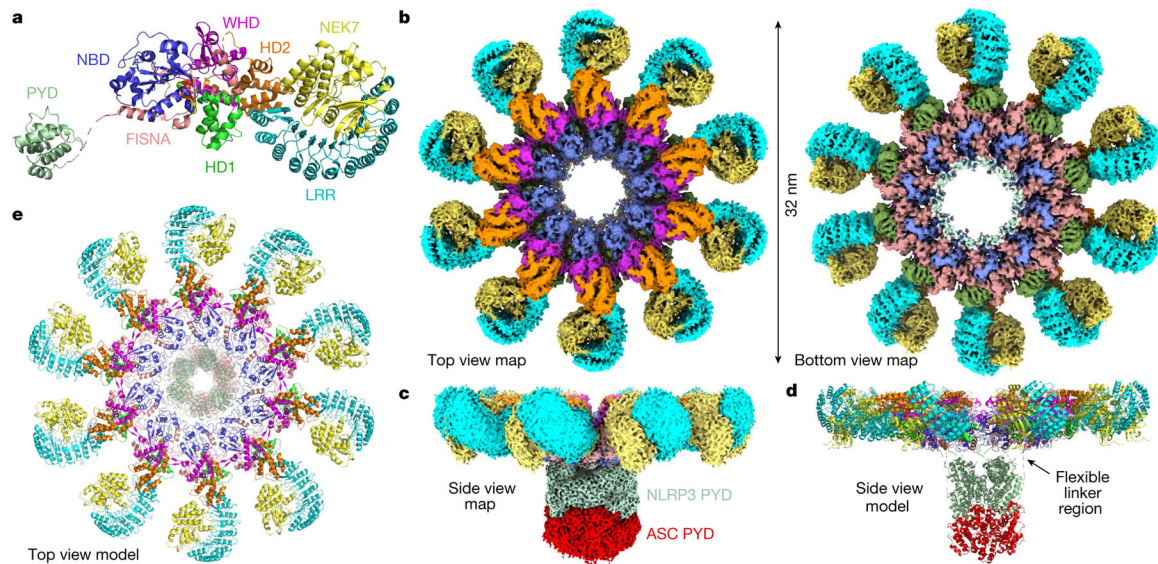
Fig. 2 |. Cryo-EM structure of the C10 NLRP3–NEK7–ASC inflammasome complex.
a, An NLRP3–NEK7 subunit coloured by domains as in Fig. 1a. The position of the PYD is somewhat arbitrary because of the disordered linker. The bound Mg–ATPγS is shown in spheres with Mg^{2+} in lemon green, carbon atoms in yellow, oxygen atoms in red, nitrogen atoms in blue and sulfur atoms in bright orange. **b**, Top and bottom views of the C10 NLRP3–NEK7–ASC complex cryo-EM map coloured by domains. **c**, Side view of the C10 NLRP3–NEK7–ASC complex cryo-EM map, highlighting the density for ten NLRP3 PYD and ten ASC PYD. **d**, Side view of the C10 NLRP3–NEK7–ASC complex model, coloured by domains. **e**, Top view of the model of the C10 NLRP3–NEK7–ASC complex, also in domain colours.
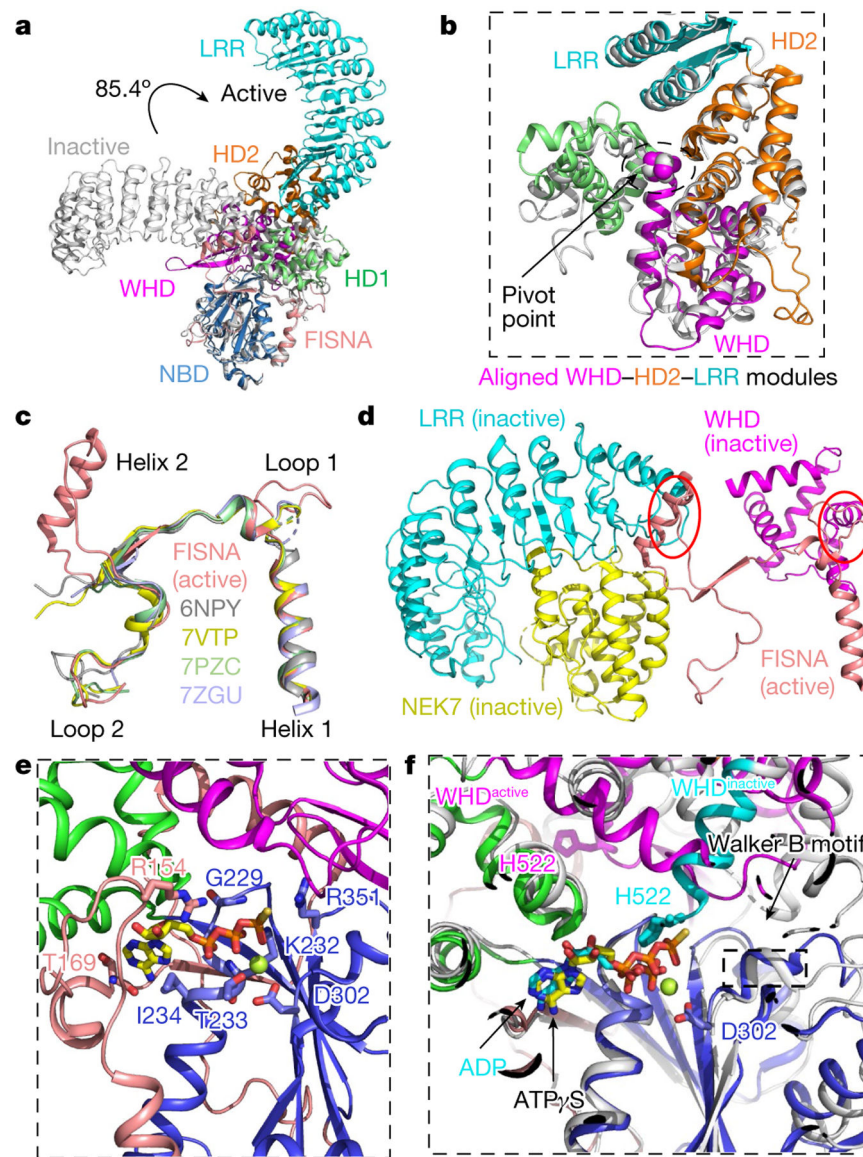
Fig. 3 |. Conformational activation of the NLRP3 inflammasome.

a, Superposition of active NLRP3 (in domain colours) and inactive NLRP3 (PDB: 6NPY in grey) by the FISNA–NBD–HD1 segment, showing overall similarity in the FISNA–NBD–HD1 region and rigid body rotation of the WHD–HD2–LRR segment. **b**, Superposition of active NLRP3 (in domain colours) and inactive NLRP3 (grey) by the WHD–HD2–LRR segment, showing overall similarity in this region. **c**, The active FISNA domain aligned with those in inactive NLRP3 structures (PDB: 6NPY, 7VTP, 7PZC and 7ZGU), showing the ordering of loop 1 and helix 2 and the conformational change at loop 2. **d**, Loop 1 and helix 2 in the active FISNA domain clash with WHD and LRR, respectively, in the inactive state. **e**, ATPγS interacts with both the FISNA domain and NBD. Mg^{2+} is shown in lemon green. **f**, Superposition of active NLRP3 and inactive NLRP3 (PDB: 6NPY in grey and cyan) showing the positions of ATPγS (carbon atoms in yellow) and ADP (carbon atoms in

cyan), respectively. H522 of the WHD of inactive NLRP3 (cyan) would have clashed with the bound ATPγS.
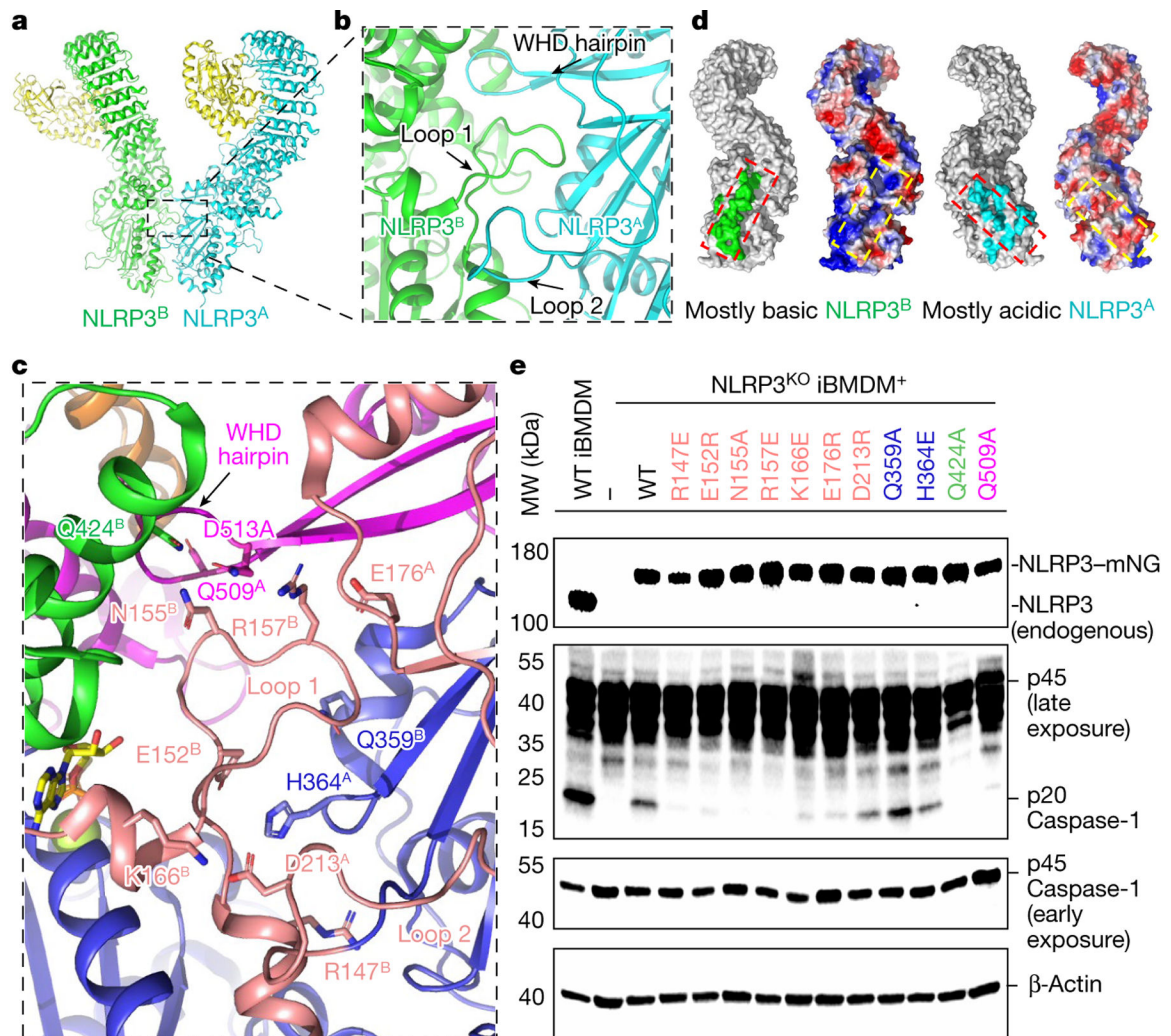
Fig. 4 |. Interaction surfaces in the NLRP3 oligomer.

a, Ribbon diagram of two neighbouring NLRP3–NEK7 subunits, shown with NLRP3^B in green and NLRP3^A in cyan. **b**, Close-up view of the interacting loops from two adjacent NLRP3 molecules. **c**, Interaction details for two neighbouring NLRP3 molecules. Ribbon diagrams and residues are coloured by domains. **d**, Mapped interactions at the NLRP3^B surface (green) and NLRP3^A surface (cyan), and their surface electrostatic potentials. Dashed rectangles denote approximate locations of the surfaces. **e**, Caspase-1 processing by WT iBMDMs and NLRP3$^{-/-}$ iBMDMs reconstituted with WT or mutant NLRP3 following LPS priming and nigericin treatment. These experiments were repeated twice. KO, knockout; mNG, mNeonGreen; MW, molecular weight.
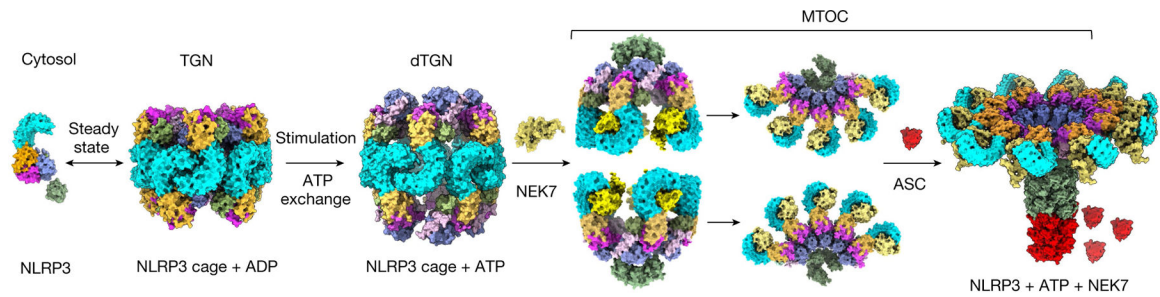
Fig. 5 |. A structure-derived model of NLRP3 inflammasome activation.
At a steady state after priming by TLR ligands such as LPS, upregulated NLRP3 is localized both in the cytosol and on the TGN in monomeric and cage forms, respectively. On stimulation, NLRP3 most probably undergoes conformational changes in the cage form and the TGN disperses into vesicles. These NLRP3-containing vesicles are trafficked on microtubules to the MTOC, where the centrosome-localized protein NEK7 interacts with NLRP3 to open the cage into two halves, possibly leading to immediate rearrangement into active NLRP3 oligomers. Recruitment of ASC then helps to complete NLRP3 disc formation and transduce the activation signal. dTGN, dispersed TGN.

Extended Data Table 1 |

Cryo-EM structure determination

	NLRP3-NEK7 (decamer)	NLRP3 PYD filament
Data collection and processing		
Nominal Magnification	81,000	
Voltage (keV)	300	
Electron exposure (e^-/Å^2)	50.4	
Defocus range (μm)	−1.0 ~ −2.0	
Pixel size (Å)	1.06	
Initial particle images (no.)	808,941	
Final particle images (no.)	51,576	33,227
Symmetry imposed	C10	C3, Helical
Map resolution (Å)	3.4	3.3
FSC threshold	0.143	0.143
Map resolution range (Å)	2.8–6.0	3.0–5.0
Refinement		
Initial model used	6NPY/2WQM	3QF2
	AlphaFold	
Model resolution (Å)	3.4/3.9	3.3/3.6
FSC threshold	(0.143/0.5)	(0.143/0.5)
Model resolution range (Å)	60–3.4	60–3.3
Map sharpening B factor (Å^2)	−112	−125.7
Model composition		
Non-hydrogen atoms	100,240	16,359
Protein residues	11,110	1995
Ligands	20	0
B-factors(Å^2)		
Protein	142.08	144.42
Ligand	106.62	
R.m.s. deviations		
Bond lengths (Å)	0.004	0.004
Bond angles (°)	0.693	0.943
Validation		
MolProbity score	2.93	2.03
Clashscore	55.44	10.38
Poor rotamers (%)	1.95	0
Ramachandran Plot		
Favoured (%)	92.15	91.86
Allowed (%)	6.94	8.09
Disallowed (%)	0.91	0.05

Data collection, refinement, and validation statistics are shown.